Thermal Modeling of Aluminum Electrolytic Capacitors

Sam G. Parler, Jr.
Cornell Dubilier
140 Technology Place
Liberty, SC 29657

Abstract – **A comprehensive thermal model for screw-terminal aluminum electrolytic capacitors is developed. The test methodology and data upon which the model is based are discussed. Exact one-dimensional solutions, multi-dimensional heat equations, and finite-element analysis (FEA) model simulation results are presented. The effects of conduction, heat sinking, natural (free) convection, forced convection, and radiation are quantified and compared. Complex issues, such as anisotropism and multi-phase heat transfer, are discussed. A comparison of model results to test data is presented. Varying capacitor construction techniques are evaluated.**

I. INTRODUCTION

The life of an aluminum electrolytic capacitor varies exponentially with temperature, approximately doubling for each 10 ºC cooler the hottest place in the capacitor (the "core" or "hot spot") is operated [1]. Since the temperature rise of the core is directly proportional to the core-to-ambient thermal resistance, the life is also an exponential function of the thermal resistance. In this paper, models to predict this thermal resistance for various construction techniques are developed and used.

This paper focuses on modeling computergrade, or screw terminal, capacitors. However, the concepts can be applied to other aluminum electrolytic capacitor constructions, such as snap-mount, radial, and axial capacitors.

An aluminum electrolytic capacitor is generally comprised of a cylindrical winding ("section") of aluminum anode and cathode foils separated by papers impregnated with a liquid electrolyte, usually based on ethylene glycol. See Fig. 1. The anode and cathode foils are made of aluminum, and the anode is usually highly etched. There is a thin coating of aluminum oxide on the surface of the anode. The anode and cathode foils are contacted by means of aluminum tabs that are extended from the winding. These tabs are attached to aluminum terminals in a polymeric top. The wet winding is sealed into an aluminum can.

One fact that is apparent when beginning the task of thermally modeling an aluminum electrolytic capacitor in a typical operating environment is that the effort is inherently complex. This complexity is due to several factors. First, all three of the heat transfer modes (conduction, convection, and radiation) are present and may be significant. Second, the conduction from the winding to the case is dependent on the method and intimacy of contact between the two. Third, as will be discussed later, the conductivity of the winding is different in the axial and radial directions. Fourth, both free convection of electrolyte-air vapor as well as two-phase heat transfer mechanisms may be present internally. Finally, external to the capacitor, both radiation and convection are present as heat transfer modes, the latter of which may be natural or forced, or both.

We undertake this work by first looking at the simpler conduction and convection aspects of the problem. We use some mathematical and FEA simulation techniques to compare predictions of simpler models with measurements taken on capacitors of known construction operating with known ripple power in known thermal environments.

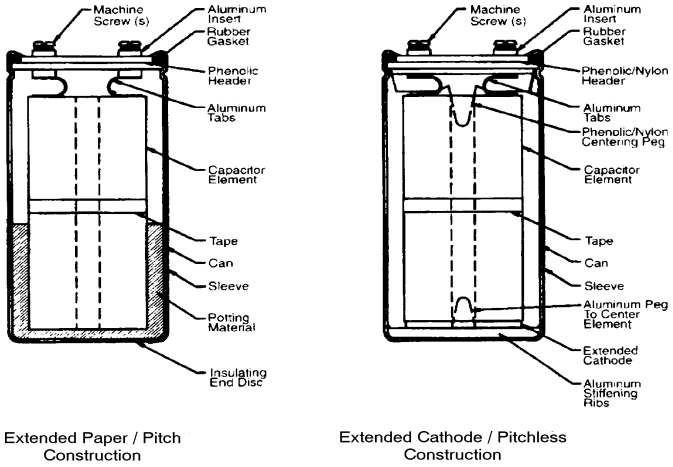

Fig. 1. Typical screw terminal capacitor constructions: pitch (left) and pitchless (right).

Presented at the IEEE Industry Applications Society Conference, October 1999

II. The winding

Starting from the hottest spot and working outward, we find that the winding of an aluminum electrolytic capacitor is highly anisotropic, due to the fact that the thermal conductivity is much larger in the axial direction than in the radial direction. This is because the papers are effectively in parallel in the axial direction but in series in the radial direction, and the conductivity of the foil is much higher than that of the papers, even when the papers are wet with electrolyte. See Table I [2]. On the other hand, the cross-sectional area of the heat flux path is generally larger in the radial direction, and the heat flux path distance is usually smaller in the radial direction, depending upon the aspect ratio (length/width ratio) of the capacitor winding. Both of these heat path geometric facts favor relatively higher thermal conductance in the radial direction, while the anisotropism greatly favors higher thermal conductance in the axial direction.

Considering a general three-dimensional physical model of the capacitor winding, we find that the symmetry lends itself to cylindrical coordinates involving an axial component z, a radial component r, and an angular component ψ. It is hoped that the thermal conductivity can be modeled as an anisotropic cylinder with no angular variation, so that ψ may be neglected. Furthermore, it is desirable to assume position-independent, constant axial and radial thermal conductivities. This is equivalent to modeling the capacitor winding axisymmetrically as a series of concentric cylinders, alternating foil and wet paper. However, we realize that there is a turn-to-turn angular contribution of the foil to the radial conductivity. This contribution diminishes as the radial position is increased. See Fig. 2.

Table I
Thermal Conductivity of Selected Materials

Material	k (W/m·K)
Type IIa Diamond	2300
Silicon Carbide	490
Silver	425
Copper	398
Aluminum	240
Aluminum Oxide	36
Ice	2.0
Pyrex Glass	1.4
Water	0.65
Silicone Rubber	0.35
Ethylene Glycol	0.26
Air or steam	0.03

To justify the assumption of a negligible angular coupling contribution to the radial thermal conductivity, we consider a single representative turn of a foil-paper layer in the winding, and compare the magnitudes of the radial thermal resistances through the bulk versus along the angular direction. See Fig. 3. We may assume that the angular conductivity k_ψ is approximately that of aluminum, that the radial conductivity k_r is approximately that of the electrolyte, and that the aluminum plate thickness and paper thickness are approximately the same, $\Delta r/2$. Since $k_\psi >> k_r$, the radial thermal resistance of this arbitrary turn is

$$\theta_r \approx \Delta r / (4\pi R L k_r), \quad (1)$$

the angular contribution to the radial thermal resistance is

$$\theta_\psi \approx 4\pi R / (\Delta r L k_\psi), \quad (2)$$

and the ratio of these thermal resistances is

$$\theta_\psi / \theta_r \approx (4\pi R / \Delta r)^2 \times (k_r / k_\psi) \ . \quad (3)$$

Noting that the paper thickness is approximately 100 μm, the radial position R of concern is at least 1 cm, and k_ψ exceeds k_r by less than three orders of magnitude, we find that the ratio (3) evaluates to at least 1600. Therefore the angular contribution of the thermal conductivity is negligible, and so the radial variation of the radial thermal conductivity is negligible. By further appealing to the symmetry of the winding, we can demonstrate that the axial conductivity k_z and the radial conductivity k_r can be assumed to be constant.

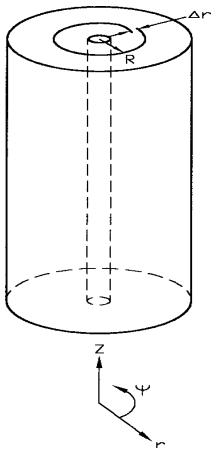

Fig. 2. Angular contribution to the radial thermal conductivity.

Presented at the IEEE Industry Applications Society Conference, October 1999

We would like to use k_r and k_z as average values for a given winding. These values need to take into account the relative thicknesses of the foil and of the paper. One complication with simply calculating the k parameters as weighted averages is that the anode foil is typically highly etched, and is often about 70% aluminum by weight and 30% aluminum oxide by weight when dry. By volume, the anode foil is only about 50% aluminum, the other components being aluminum oxide and electrolyte. Obviously we cannot simply use the percentage of aluminum to calculate the relative values of the axial and radial thermal conductivities of the anode foil, since the etching geometry is the more dominant factor and is not uniquely determined by the aluminum volume.

Another complicating factor in calculating the axial and radial thermal conductivities is the paper compression that occurs in an actual winding. It is difficult to know the compressive force on a paper as it is wound, and even more difficult to estimate this after the winding is saturated with electrolyte, causing the paper to swell.

Because of these complicating factors and since we want to measure the thermal conductivities of other materials used in the construction of capacitors, we measure the thermal conductivities empirically on a thermal test stand. Fig. 4 shows a schematic of the test setup we use. A material of thermal conductivity k, uniform length L, and uniform cross-sectional area A has a thermal resistance along its length of

$$\theta = L / (kA). \quad (4)$$

The temperature drop ΔT across a thermal resistance θ with a power P flowing through it is

$$\Delta T = P\theta = PL / (kA). \quad (5)$$

Therefore the thermal conductivity can be determined as

$$k = PL / (A\Delta T). \quad (6)$$

This simple relationship was used to determine thermal conductivities of a wide variety of capacitor materials and of the axial thermal conductivity k_z of the winding itself. Windings of various sizes were drilled at 1 inch axial spacing approximately 0.5 inches deep, and thermocouples were inserted into these holes. The injected power P was adjusted from 5 watts to 20 watts through use of a silicone rubber heater clamped between thin aluminum plates. The power source was an AC variac, and a power meter was used to measure the dissipated power. The plate was pressed in contact with the top of the wet winding, and the bottom of the winding was placed in contact with a flux-measuring device comprised of two parallel aluminum plates with a vacuum casting of a polymer with known thermal conductivity. The other side of the flux measuring device was thermally bonded to an aluminum chiller plate of programmable temperature.

The entire system was enclosed in a large silicone foam rubber cylinder full of styrofoam pellets to create a nearly adiabatic environment. A computer and data acquisition system

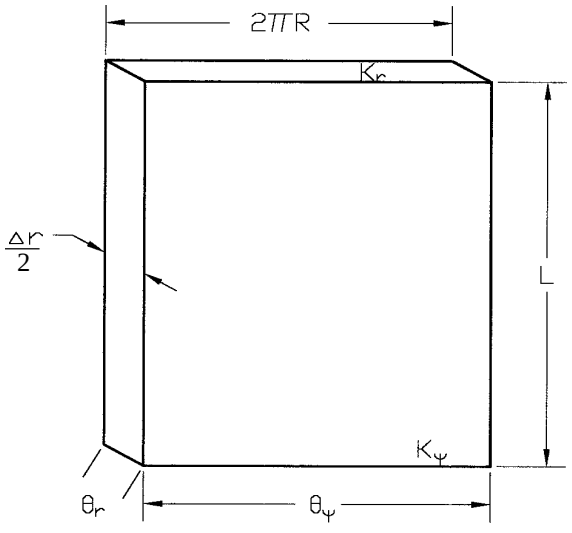

Fig. 3. Angular contribution to the radial thermal conductivity of an arbitrary turn at radial location R.

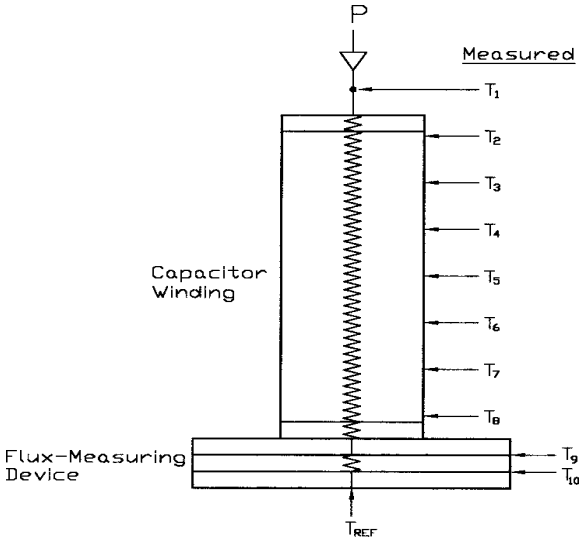

Fig. 4. Measuring the axial thermal conductivity of a capacitor winding.

Presented at the IEEE Industry Applications Society Conference, October 1999

were used to monitor the temperatures under each test condition. Generally, steady-state conditions were reached within four hours.

Measuring the radial thermal conductivity was somewhat more complex than measuring the axial thermal conductivity for two reasons. First, a radial heat source to make intimate contact with the arbor hole was not easy to design and fabricate. It was necessary to use an expanding copper arbor with thermally bonded resistors. Secondly, the radial heat flow path prevented (6) from being used, since the cross-sectional area varied with the radius. An expression for the thermal conductivity versus power, length, and radial position is derived as follows. Let P represent the uniformly injected power into a cylindrical region of radius R_I centered along the axis of a cylindrical winding whose outer radius is R_O and whose radial thermal conductivity is k_r. The outer surface $r=R_O$ of the winding is maintained at temperature T_O. See Fig. 5. The temperature distribution is readily derived by using a variation of (5), where we consider the length to be an incremental radius $d\lambda$ and the cross-sectional area to be a function of the radius λ,

$$A(\lambda) = 2\pi\lambda L, \tag{7}$$

Since we know the temperature at $r=R_O$, we have

$$T(r) = T_O + \int_r^{R_O} \frac{P \cdot d\lambda}{2\pi k_r \lambda L}, \tag{8}$$

which simplifies to

$$T(r) = T_O + P \cdot \ln(R_O/r)/(2\pi k_r L). \tag{9}$$

Equation (9) assumes that there is no axial heat loss.

Radial thermal tests were performed on a 2.5” diameter by 5” long winding with a 0.75” diameter hole bored along its axis. Thermocouples were inserted into small holes drilled at 0.25” intervals, approximately 1.5” deep, at various radial locations. The winding was impregnated with pure ethylene glycol (the nonconductive, common electrolyte solvent) instead of electrolyte to prevent ionic contamination of the copper power resistor assembly. A large, flanged, four-piece, hollow aluminum cylinder with 0.75” thick walls was used to make contact between the outside of the winding and the flat chiller plate during these tests. The four sides of the block were clamped with large hose clamps to establish good thermal contact to the outside of the wet winding. The entire system was thermally isolated as in the previous tests.

The temperature distribution was recorded on the data acquisition system, and the temperatures were found to fit a logarithmic plot that conformed to (9) almost perfectly. See Fig. 6. The power was varied from 10W to 20W and the chiller reference temperature was varied from 25 ºC to 65 ºC. The value of k_r was deduced from these measurements and was found not to vary by more than ±10% over the tested range.

Additional measurements were made of stacks of wet capacitor paper materials, of the sleeve materials, of pitch materials, and of contact resistances between the wet capacitor winding and the can bottom versus applied force.

Table II summarizes the measured values of thermal conductivities. We want to use these values in a thermal model, but we also want to be able to evaluate various sizes, shapes, and construction techniques interactively. For example, what is the effect of thickening the can bottom, installing an aluminum rod through the center of the capacitor, using an aluminum top, etc. Before we can answer these questions, we need to

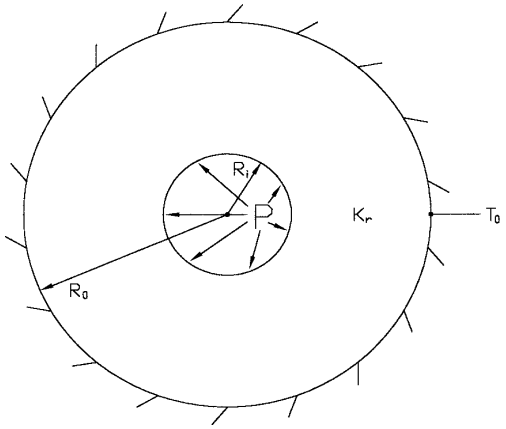

Fig. 5. Measuring the radial thermal conductivity of a capacitor winding.

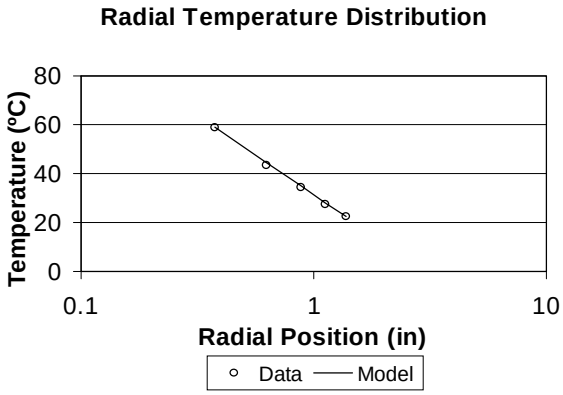

Fig. 6. Model and data of the radial temperature distribution of a capacitor winding with power injected at the arbor.

Presented at the IEEE Industry Applications Society Conference, October 1999

develop a model of how heat is transferred throughout the winding when the power generation is uniform rather than concentrated at an artificially established isothermal surface as in the thermal conductivity measurement experiments. Additionally, we need to determine how the heat is transferred from the capacitor winding to the can, and from the can to the environment. Also, we want a fast, interactive thermal model.

The general heat equation is

$$\nabla^2 T + \frac{g}{k} = \frac{\delta C_p}{k} \bullet \frac{\partial T}{\partial t} \qquad (10)$$

where ∇^2 is the Laplacian operator, T is the spatial temperature distribution, δ is the material density, k is the material thermal conductivity, g is the regional volumetric power density, C_p is the specific heat, and t is time.

When the steady-state solution is sought, the transient term on the right-hand side of (10) is zero. In rectangular coordinates, the steady state, one-dimensional heat equation is

$$\frac{\partial^2 T}{\partial z^2} + \frac{g}{k} = 0 \ . \qquad (11)$$

The solution for the axial temperature distribution of a winding whose power is removed through conduction through its bottom end to a reference environmental temperature T_1 is straightforward. See Fig. 7. In this case, g = P/(AL), and, integrating (11) twice with respect to the axial coordinate z, we obtain

$$T = C_1 z^2 + C_2 z + C_3 \ . \qquad (12)$$

To obtain the value of the three constants, we need to use three boundary conditions. We know that since the total power flows through the thermal resistances to the reference temperature,

$$C_3 = T(0) = T_1 + P\,(\theta_1 + \theta_2)\,. \qquad (13)$$

Furthermore, by Fourier's Law [3] at the bottom, we know that

$$C_2 = \left.\frac{dT}{dz}\right|_{z=0} = \frac{P}{k_z A} \ . \qquad (14)$$

Finally, applying Fourier's Law at the top, we obtain

$$\left.\frac{dT}{dz}\right|_{z=L} = 0 = 2C_1 L + C_2 \ . \qquad (15)$$

which yields

$$C_1 = -P / 2k_z LA \ . \qquad (16)$$

In a similar manner, we may solve for the radial temperature distribution of a winding with uniform power generation and whose heat is removed solely in the radial direction. See Fig. 8. We first examine the steady state heat equation in cylindrical coordinates:

$$\frac{1}{r} \bullet \frac{d}{dr}\left[r \frac{dT}{dr}\right] + \frac{g}{k_r} = 0 \ . \qquad (17)$$

Here

$$g = P / [\pi(R_O^2 - R_I^2)L] \ . \qquad (18)$$

Table II
Measured Thermal Conductivities

Material	k (W/m·K)
k_z	100
k_r	0.21
Dry Paper (0.35 g/cm^3)	0.046
Dry Paper (0.55 g/cm^3)	0.055
Dry Paper (0.90 g/cm^3)	0.076
EG-Impregnated paper	0.17 - 0.20
PVC Sleeve Material	0.093
End Disc Material	0.089
Sil Pad Material	0.34
Pitch	0.35

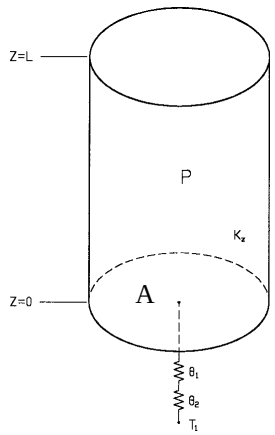

Fig. 7. Deriving the axial temperature distribution of a capacitor winding with uniform power generation.

Presented at the IEEE Industry Applications Society Conference, October 1999

Multiplying by r then integrating yields

$$r\frac{dT}{dr} = \frac{-Pr^2}{2\pi(R_O^2 - R_I^2)Lk_r} + C_4 \quad . \tag{19}$$

Dividing by r and integrating, we have

$$T(r) = \frac{-Pr^2}{4\pi(R_O^2 - R_I^2)Lk_r} + C_4 \ln(r) + C_5 \quad . \tag{20}$$

Again solving for constants by enforcing boundary conditions, we know that there is no flux or gradient at $r=R_I$. Therefore,

$$\left.\frac{dT}{dr}\right|_{r=R_I} = 0 \Rightarrow C_4 = \frac{-2PR_I^2}{4\pi(R_O^2 - R_I^2)Lk_r} \quad . \tag{21}$$

Since we know $T(R_O) = T_1 + P(\theta_1 + \theta_2)$, we have

$$C_5 = T_1 + P(\theta_1 + \theta_2) + \frac{P[R_O^2 + 2R_I^2 \ln(R_O)]}{4\pi(R_O^2 - R_I^2)Lk_r} \quad . \tag{22}$$

III. Winding To Can

At this stage we have sufficient models ((4), (9), (12) and (20)) and parametric values (Table II) to perform some comparisons between radial and axial heat transfer for a couple of different construction types and cooling techniques.

Let us first consider windings of various sizes whose lengths are three times their diameters, assuming a uniform volumetric power density $g = 10^5$ W/m^3. Fig. 9 shows the relative effect on the maximum core temperature of maintaining an isothermal surface of 25 ºC at the entire outer radial surface (radial cooling) versus contacting the bottom only (axial cooling). Here $\theta_1 = \theta_2 = 0$. It can be seen that axial cooling is much more effective than radial cooling, especially in larger capacitors.

Now let us compare axial and radial conductances by considering a more realistic case where the capacitor winding is coupled through its can which is contacting slowly moving air at a temperature T_1= 25 ºC. The winding size is 2.5" diameter by 5" length, dissipating 10 watts, and the can is 3.0" outside diameter (2.95" inside diameter) by 5.6" length. Let θ_1 represent the thermal resistance from the winding to the can, and let θ_2 = 2 ºC / W represent the thermal resistance from the can to the environmental temperature T_1. If we consider the can to be an isothermal surface, this means that the can temperature is 45 ºC.

Generally in capacitor designs with pitch or potting compound, the winding is not compressed tightly against the can bottom, causing the axial thermal resistance from the winding to the can bottom to be relatively high. In the best pitchless designs, there are reinforcement ribs and integral center spikes in the top (header) and in the bottom to keep the winding aligned and to allow high compression of the winding. The lowest axial thermal resistance from winding to case is achieved in high compression pitchless designs with extended cathode, where the cathode is wider than the anode, and is offset and exposed on the bottom of the winding, having an effective thermal conductivity that is dominated by interfacial properties (contact resistance) rather than bulk conduction properties. This interfacial conductivity was measured on the thermal test stand of Fig. 4 as being approximately 800 W/(m^{2}K). Notice the units indicate that the effective conductivity is obtained by multiplying the interfacial conductivity by the thickness of the interface.

For the case of axial conduction, we find for compressed wet paper between the winding bottom and the can, assuming a thickness of 0.062" and referring to (4) and Table II, θ_1 = 2.8

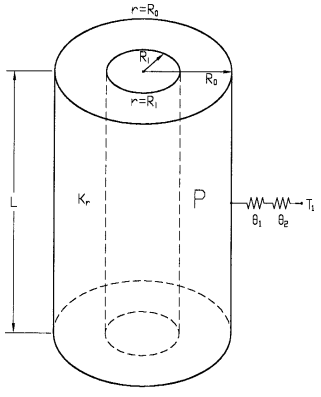

Fig. 8. Deriving the radial temperature distribution of a capacitor winding with uniform power generation.

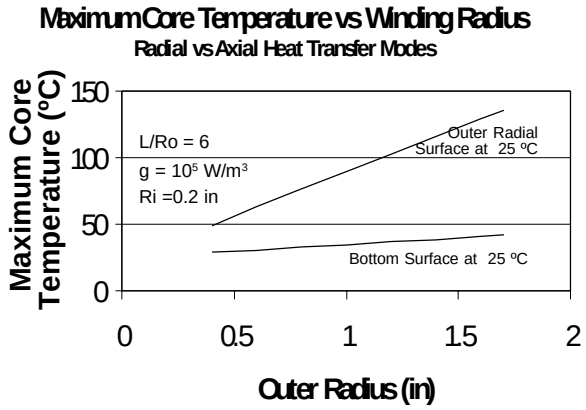

Fig. 9. Relative effects of heatsinking the outer radial surface of winding vs heatsinking the bottom of winding.

Presented at the IEEE Industry Applications Society Conference, October 1999

ºC/W; for uncompressed paper, assuming the thickness is 0.125 inches, θ_1 = 5.6 ºC/W. For compressed extended cathode winding of this size in a pitchless design, we obtain 0.4 ºC/W. Using (12), we calculate the axial thermal resistance of the winding as θ_a = 0.20 ºC/W.

In the radial direction, in a design which is half-filled with pitch, the winding-to-can thermal resistance due to the pitch is calculated using (9) as 1.2 ºC/W. We have not yet derived the expressions for coupling via free convection and radiation of the winding to the can in the case of a pitchless design, but let us take this (to be justified later) as θ_1 = 2.7 ºC/W for the entire winding to the can. Twice this thermal resistance would appear in parallel with the pitch resistance of 1.2 ºC, since the pitch only fills half of the space between the winding and can, giving a revised value of θ_1 = 1.2 // 5.4 = 0.98 ºC/W for the radial winding-to-can thermal resistance of the pitch design. Using (20) we find the radial thermal resistance of the winding to be θ_r = 3.1 ºC/W.

Employing the thermal resistances above, we obtain the results summarized in Table III. Since both radial and axial heat transfer modes are present, and the can is virtually an isothermal surface, we may approximate the simultaneous effects of both axial and radial conduction by computing the result of the axial and radial thermal resistances in parallel. We conclude that the pitchless design with extended paper has a slight advantage over the pitch design, and that the extended cathode design has a very large advantage. In actual practice, the can temperature is not truly isothermal. In the case of the pitchless, extended cathode design, the can bottom is somewhat hotter than the sides, erasing some of the advantage of the pitchless design over that of the pitch design.

Even though our simple one-dimensional thermal models have already led to useful results, showing that axial conduction offers the best opportunity for heat removal and allowing us to quantify the effects of heatsinking, we have so far only considered axial and radial thermal conductivity separately, and then lumped the average thermal resistances in parallel to examine the simultaneous effect. To precisely model the axial and radial heat conduction, we need to revisit (10). In cylindrical coordinates, for the steady-state solution, we multiply by k to obtain

$$\frac{k}{r} \bullet \frac{\partial}{\partial r}\left[r \frac{\partial T}{\partial r} \right] + k \frac{\partial^2 T}{\partial z^2} + g = 0 . \qquad (23)$$

Since we are considering an anisotropic medium, we must associate the axial and radial conductivities separately. Fortunately, (23) is in a separable form with respect to the spacial variables and this is straightforward. We have

$$\frac{k_r}{r} \bullet \frac{\partial}{\partial r}\left[r \frac{\partial T}{\partial r} \right] + k_z \frac{\partial^2 T}{\partial z^2} + g = 0 . \qquad (24)$$

Unfortunately, (24) is impossible to solve in closed form for most interesting cases. If we assume g=0 (no internal power generation) and provide surfaces with simple boundary conditions, we obtain solutions of the form

$$T(r,z) = \sum_i^\infty \sum_j^\infty \left\{ \left[a_i J_0\left(\frac{\lambda r}{\sqrt{k_r}}\right) + b_i Y_0\left(\frac{\lambda r}{\sqrt{k_r}}\right) \right] \bullet \left[c_j J_0\left(\frac{\lambda z}{\sqrt{k_z}}\right) + d_j Y_0\left(\frac{\lambda z}{\sqrt{k_z}}\right) \right] \right\} , \qquad (25)$$

where J_0 and Y_0 are the zeroth-order Bessel and Weber functions, respectively. It was therefore concluded fairly early in our thermal modeling development work that computer solutions would need to be employed.

Table III
Results from 1-D Models

θ_2 = 2 ºC/W, T_1 = 25 ºC, P = 10 W, 2.5" dia × 5" L winding

Construction	θ_1 r ºC/W	θ_1 z ºC/W	Heat Flow Direction Radial T_{CORE}	Axial T_{CORE}	r // z T_{CORE}
Pitch	0.98	5.6	86 ºC	103 ºC	67 ºC
Pitchless, Extended Paper	2.7	2.8	103	75	65
Pitchless, Extended Cathode	2.7	0.4	103	51	50

IV. Can To Environment

The heat transfer modes from the can to the ambient environment may include conduction, convection, and radiation. Conduction is a volumetric parameter, and includes path length as well as cross-sectional area effects, as has already been discussed. Externally, conduction is a significant mode only when the capacitor is attached to a heat sink.

Convection, on the other hand, is generally modeled as a surface effect, although the localized film thickness and velocity (hydrodynamic) and temperature (thermodynamic) distributions extend beyond the surface. The parameter that describes the degree of thermal heat transfer coupling from a surface of

Presented at the IEEE Industry Applications Society Conference, October 1999

area A to the ambient fluid is known as the convection or film coefficient, h, which is a strong function of the fluid velocity and mass transfer properties, such as density and viscosity. If the surface is at a higher temperature than the environment by an amount ΔT, the power P_{CONV} dissipated through convection is given by

$$P_{CONV} = hA\Delta T. \quad (26)$$

Although (26) holds for virtually any fluid, this paper deals only with the fluid being air at standard atmospheric pressure and at a temperature between 25 ºC and 85 ºC.

An approximate value of h versus velocity which is commonly used in the capacitor industry is

$$h_{TOT} \approx 11 \sqrt{(v+0.25)/(0.25)}\ [W/m^2K] \quad (27)$$

where the velocity v is in units of [m/s]. Other sources also use a square-root dependence of h on airstream velocity [4,5]. We note that h has the same units as the interfacial conductance, and analogously, is also associated with a thickness (the "film" thickness) to calculate a relevant thermal conductivity. The film thickness is not used directly in our calculations, but it varies from about 3 cm in natural convection to less than 1 mm in high-velocity air flows [6].

Equation (27) lumps together the effects of natural (free) convection, forced convection, and radiation. The velocity of "still" air, or natural convection, is taken as 0. The equation above does not take into account many factors, such as capacitor gravimetric orientation, the aspect ratio (D/L), the ambient and surface temperatures, laminar versus turbulent flow, etc. The results when using (27) to predict heat rise ΔT are generally within about 20% of the measured value. For more exact solutions, we need to use heat transfer theory.

Let us denote the unitless average Reynolds, Nusselt, and Rayleigh numbers as Re, Nu, and Ra, respectively. A subscript of D or L is generally used along with the numbers to indicate application to a cylinder or plate, respectively. Additionally, there is a unitless number Pr, the Prandtl number, which describes the medium. Pr is 2/3 for monatomic gasses, 5/7 for diatomic gasses, and has little temperature variation in our region of interest [7]. For airstream velocity v, cylinder diameter D, and kinematic viscosity ν,

$$Re_D = vD/\nu \quad (28)$$

and

$$Nu_D = 0.3 + \frac{0.62\ Re_D^{1/2}\ Pr^{1/3}}{[\ 1 + (0.4/Pr)^{2/3}\ ]^{1/4}} \left[1 + \left(\frac{Re_D}{28{,}200} \right)^{5/8} \right]^{4/5} \quad (29)$$

and finally

$$h = k\ Nu_D / D \quad (30)$$

for a cylinder in cross-flow, where k is the thermal conductivity of air at the film temperature, taken as the average of the surface and airstream temperatures [8]. Notice that (29) contradicts the assumption of a strictly square-root relationship between the convection coefficient and the airstream velocity.

For natural (free) convection of aluminum electrolytic capacitors,

$$h = 1.32\ (\Delta T/D)^{1/4}\ [W/m^2K] \quad (31)$$

where ΔT is the difference in temperature between the can surface and the ambient air temperature in ºC, and D is the diameter in meters [9].

Some general comments should be made about convection at this time. In general, the convection coefficient h is somewhat larger for small capacitors than for large ones, especially for free convection, as indicated in (31). Over the size range of aluminum electrolytic screw terminal capacitors, h may be up to 40% higher for the smallest caps (35 × 40 mm) than for the largest capacitors (90 × 220 mm), due to size alone. Also, h for forced air decreases slightly at elevated temperatures, due to the positive temperature coefficient of the ν factor, which increases about 0.5%/ºC [2]. There is some gravitational dependence, but it has been found by this author to be slight.

Radiation, like convection, is also a surface-to-environment effect. The radiation heat transfer is dependent not only on the temperature difference between a surface and its environment, but also on the absolute temperatures involved. The surface "darkness" or emissivity ε is also important in radiation heat transfer. The power P_{RAD} transferred from a surface area A at temperature T_S to an environment at temperature T_∞ due to radiation is

$$P_{RAD} = \varepsilon\sigma A\ (\ T_S^4 - T_\infty^4\ ) \quad (32)$$

where ε is the surface emissivity (0-1) or "darkness" in the infrared region of the electromagnetic spectrum, and $\sigma = 5.67 \times 10^{-8}$ W/m^2K^4 is the Stefan-Boltzmann constant [9]. For sleeved capacitors, $\varepsilon = 0.85$ is a good approximation [9]. For

bare capacitors, $\varepsilon = 0.4$ approximately [9]. Equation (32) may be put into a form equivalent to (26) by factoring out $\Delta T = (T_S - T_\infty)$, yielding

$$P_{RAD} = h_{RAD} A \Delta T \quad (33)$$

where

$$h_{RAD} = \varepsilon\sigma(T_S + T_\infty)(T_S^2 + T_\infty^2). \quad (34)$$

It can be seen from (34) that the radiation coefficient h_{RAD} increases with both increasing surface and environmental temperatures, and it increases slightly as the ΔT is increased while maintaining the same average temperature. This effect is often offset by the decrease in h (convection) with increasing temperature when both radiation and convection are significant heat transfer modes.

Radiation heat transfer can be significant compared to natural convection alone. Generally, the convection coefficient h for natural convection varies from about 5 to about 7 W/m^{2}K, while h_{RAD} varies from about 5 to 9 W/m^{2}K for capacitors of this size and temperature range. This gives a total h range for natural convection plus radiation of about 10 to 15 W/m^{2}K, agreeing with (27).

Fig. 10 compares the values of h found for actual capacitors under natural convection conditions versus the model resulting from adding (31) and (34). Fig 11 compares the values of h found for capacitors under forced convection conditions compared to (27) and to (30) evaluated at two diameters. A new model is proposed as

$$h_{TOT} = 5 + 17 (v + 0.1)^{0.66} \quad (35)$$

and this is also shown in Fig. 11.

V. Other Internal Considerations

Now that we have discussed both radiation and natural convection, we may consider their combined effects in radially coupling the outer surface of the winding to the inside of the can wall. If we assume the outer surface of the winding of radius R_W and length L to be at absolute temperature T_W and to have an emissivity of $\varepsilon_W = 0.85$, and the inner surface of the can of radius R_C to be at absolute temperature T_C and have an emissivity of $\varepsilon_C = 0.40$, we may calculate the transferred power via radiation [10] as

$$P_{RAD} = \frac{\sigma A (T_W^4 - T_C^4)}{\frac{1}{\varepsilon_W} + \frac{1-\varepsilon_C}{\varepsilon_C}\left[\frac{R_W}{R_C}\right]} \quad . \quad (36)$$

We may also calculate the power transferred from the winding radially to the can wall via convection by using [11]

$$k_{EFF} = 0.386\, k_{AIR} [PrRa_C / (0.861+Pr)]^{1/4} \quad (37)$$

where K_{AIR} is the conductivity of still air, and

$$Ra_C = 8Ra_L [\ln(R_C / R_W)]^4 / [L^3 (R_C^{-3/5} + R_W^{-3/5})^5] \quad (38)$$

where R_C is the inner radius of the can wall, R_W is the outer radius of the winding, $L = R_C - R_W$, and Ra_L is given by

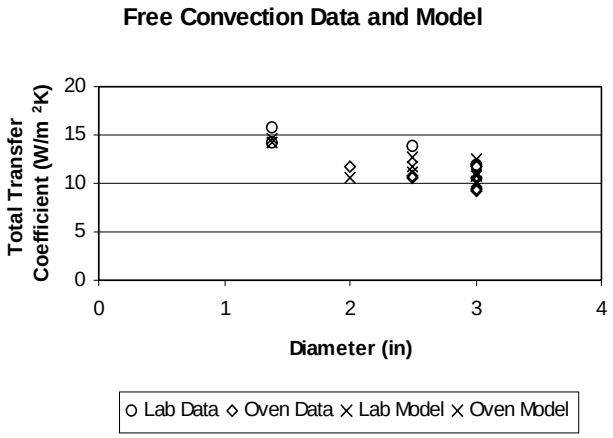

Fig. 10. Data and model for total heat transfer coefficient h versus diameter for natural convection cooling.

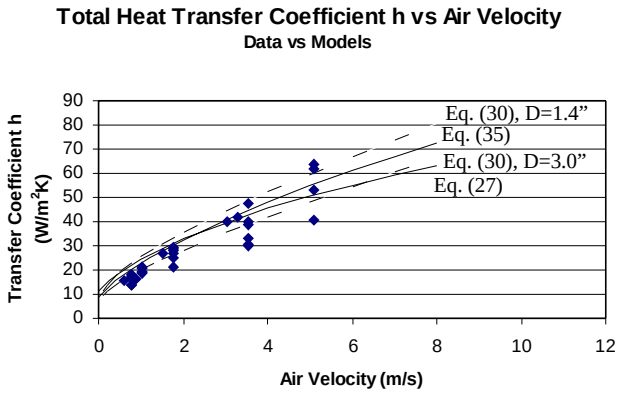

Fig. 11. Data and model for total heat transfer coefficient h versus air velocity for convection cooling.

Presented at the IEEE Industry Applications Society Conference, October 1999

$$Ra_L = gL^3/(T_F \nu \alpha) \quad (39)$$

where T_F is the absolute film temperature and α is the thermal diffusivity, which has about the same temperature coefficient as the kinematic viscosity ν. Equation (37) is recommended for use in the range of $10^2 < Ra_L < 10^7$, but has been found by this author to give reasonably accurate estimates below the lower range. After examining the combined effects of (36) and (37) for capacitors of the sizes and temperatures under consideration, this author suggests using a simplified combined radial transfer thermal conductivity of

$$k_{RWC} = 0.030 + 1.3 \frac{\sigma R_W (T_W^4 - T_C^4) \ln(R_C / R_W)}{\left[\frac{1}{\varepsilon_W} + \frac{1-\varepsilon_C}{\varepsilon_C}\left[\frac{R_W}{R_C}\right]\right]\Delta T} \quad . \quad (40)$$

Another postulated contributing factor to promoting radial heat transfer from the winding to the case as well as possibly increasing the effective axial thermal conductivity of the can wall is the so-called “heat pipe” effect, which is augmented heat transfer due to phase change of the electrolyte. The effect has a gravitational dependency, and is most effective when used with a fluid with a large latent heat of vaporization which evaporates and condenses readily at the device and heatsink temperatures, respectively. Heat pipes transfer heat most readily from a hot area (heat source) below a cooler area (environment), and can achieve extremely high effective thermal conductivity, over 100 times that of silver [12]. Because this effect was potentially significant but was difficult to calculate, we decided to measure it experimentally using a thermal conductivity test stand similar to that of Fig. 4. We measured the can wall conductivity of a 3” diameter by 8.63” length, empty capacitor, sealed with a capacitor top and gasket. Then we punctured the side wall, injected approximately 10 cm^3 electrolyte, resealed the can, and measured the thermal conductivity again. We performed the same procedure for a capacitor that was empty except for a single turn of foil taped to form a hollow cylinder of approximate size 2.7” diameter by 5” length. We wrapped several turns of capacitor paper around the hollow form to produce a wick. We also measured capacitors of the same size with large and small winding diameters. To summarize the results, we found an improvement in axial conductivity of only 10 - 25 % in this series of experiments.

VI. Other External Considerations

The test stand of Fig. 4 was used to measure interfacial conductivities between the can and a heatsink. These data are summarized in Table IV. The forces are based on the calculations from the torque applied to the 4 threaded rods used to clamp the capacitors to the chiller plate.

It is postulated that the air trapped between the capacitor and the chiller plate gives rise to the largest effects that are observed. The flatness of the capacitor can bottom is also important and presumably interacts with the clamping technique employed. For example, if the capacitor bottom surface were concave, clamping via the can walls would not be as effective in driving out the air pockets as mounting via a stud in the center of the can bottom.

Although a bare aluminum capacitor can offers the highest interfacial conductance from the can bottom to the heat sink, generally, electrical isolation is needed between these two surfaces. In this case, the best thermal interfacial conductance is achieved with a Sil-Pad Material or with thermal grease, along with flat surfaces and at least 20 pounds of force per square inch of can bottom area.

VII. Model Results

Early in this project we were using a finite-element analysis (FEA) software package which did not allow direct simulation of anisotropic material properties. Instead, a large number of individual paper and foil layers had to be drawn. A change in construction (paper thickness, capacitor length, etc.) usually required a complete redraw, taking two hours. Rerunning the software for a new condition took about 20 minutes. This meant we could run about 4 simulations per day. For these reasons, this author began investigating other alternatives and decided the best solution was to automatically draw the capacitor and

Table IV
Measured Thermal Contact Resistances
3-inch Diameter Capacitor Bottom to Flat Plate

Force (lbs)	*Sleeve/ End Disc*	*Bare Aluminum*
0	1.62 ºC/W	0.62
90	1.30	0.33
180	1.22	0.33
360	1.12	0.30
	Sleeve/ End Disc/ Sil Pad	*Bare Aluminum plus Sil Pad*
0	1.52	0.62
90	1.20	0.48
180	1.13	0.42
360	1.07	0.40

solve the partial differential equations and boundary conditions with an FEA equation solver.

The equation solver we use allows the capacitor to be "drawn" by connecting coordinates with line segments and arcs. Each component of the capacitor— the can, the bottom of the winding, the inactive turns (with no anode) at the arbor, the active winding, the top of the winding, the header, the header ribs, the dead space around the winding, the dead space in the arbor, the sleeve, the end disc, etc., are all drawn symbolically with their dimensions as user-editable inputs in the text-based source file. Axial and radial conductivities are assigned to each of the components, as are any boundary conditions, such as flux at the outer edge of the sleeve, end discs, and top. The main advantage of this approach is the speed with which modifications are made and evaluated. For example, to evaluate a sleeve thickness change, only the sleeve thickness dimension needs to be edited, as all other dimensions are adjusted automatically, working in from the outside dimensions, since they are variables. This change is made in about 15 seconds, and the program generally executes in about 30 seconds.

As other examples, the can bottom thickness, can wall thickness, sleeve conductivity, dead turns thickness, arbor conductivity, header conductivity, air velocity, heat sink properties, etc. are all changed and evaluated within minutes instead of hours. The output is graphical, showing a color plot of the right half of a cross-section of the axisymmetric temperature distribution. See Fig. 12.

The equations and measured values presented in this paper are used as inputs, and there appears to be good correlation between the model results and actual data. See Table V. These capacitors are all of extended cathode construction, but the model was found to fit well to capacitors of extended paper construction as well, as EC/EP (extended cathode / extended paper) is programmed as a parameter within the simulation. The model takes into account the winding diameter, which varies in this data from about 50% full to over 90% full. The model is generally within 10% of predicting the actual heat rise. The repeatability of the experimental data is not much less than 10%, especially for low air velocity and/or low heat rise. Refinement of the model and of the measurement techniques continues.

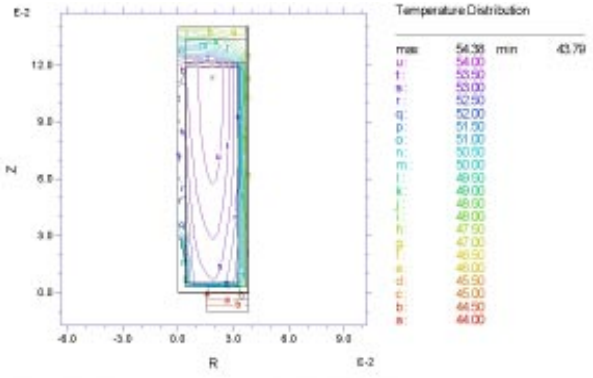

Fig. 12. Typical graphical output from thermal model. The isotherms are shown and are labeled and color-coded. This particular model has a heatsink, and 2 m/s moving air.

The relative benefit of various constructions are shown in Table VI. The base assumptions are a capacitor of can size 3" diameter by 5.625" length, dissipating 10 watts in a 45 ºC environment with an air flow velocity of 2 m/s. All of the EP simulations, including those of pitch-containing capacitors, assume the construction to be of the high-compression type, which gives a somewhat lower core-to-can-bottom thermal resistance than would be expected from a typical uncompressed pitch design. The poorest construction from a thermal standpoint is the pitchless construction with extended paper (NP/

Table V
Measured versus Modeled Temperatures
Miscellaneous Production Capacitors
(Tc and Tb are core and bottom temperatures (ºC), respectively.)

					Measured		Modeled	
D(in)	L(in)	Ta(ºC)	v(m/s)	P(W)	Tc	Tb	Tc	Tb
2.0	3.1	24.6	1.0	5.0	45.6	41.0	45.3	39.5
2.0	3.1	26.7	1.8	5.3	43.2	39.5	45.0	39.0
2.0	3.1	27.3	3.6	5.5	41.6	35.9	42.9	36.5
2.5	5.6	27.1	0.76	9.1	52.0	44.4	51.0	42.5
2.5	5.6	27.6	1.8	9.4	48.5	39.9	47.5	38.5
2.5	5.6	28.1	3.6	9.5	46.8	37.7	45.3	36.5
2.5	5.6	27.8	0.76	4.3	40.6	38.3	39.3	35.1
2.5	5.6	29.4	1.8	4.4	39.3	36.5	38.8	34.5
2.5	5.6	30.2	3.6	4.4	38.9	35.8	38.3	33.9
2.0	3.1	59.6	0.76	3.8	76.8	73.5	76.7	72.5
2.0	3.1	58.8	1.0	3.8	76.6	70.9	75.0	71.0
3.0	5.6	32.0	1.0	7.7	46.3	43.0	47.0	41.5
3.0	5.6	29.9	1.8	8.0	42.1	37.6	43.6	38.0
3.0	5.6	32.3	3.3	7.9	42.5	38.2	44.0	38.5
2.0	3.1	58.8	0.60	3.8	78.2	75.0	77.0	72.5
3.0	5.6	64.6	0.90	2.2	69.2	68.1	69.5	67.4
2.5	5.6	30.2	0.76	8.4	54.1	46.4	52.1	44.0
2.5	5.6	29.0	1.5	9.0	49.3	40.5	48.8	40.5
2.5	5.6	30.1	3.0	9.3	48.0	38.9	47.5	38.5
3.0	5.6	67.3	1.0	4.9	76.9	74.0	78.0	73.5
2.5	4.1	31.0	1.0	5.7	46.4	43.6	46.3	42.0
2.5	4.1	31.8	1.8	5.8	43.7	40.9	45.1	40.5
2.5	4.1	33.0	3.6	5.8	42.2	40.1	44.0	39.5
3.0	4.1	27.0	0.76	6.4	44.5	40.2	44.1	38.0
3.0	4.1	30.0	1.8	6.4	43.6	39.0	43.8	38.0
3.0	4.1	28.9	3.6	6.6	41.1	36.3	40.9	35.0
1.4	4.6	24.8	5.1	5.3	41.6	33.1	40.1	33.0
1.4	4.1	25.0	5.1	4.1	38.2	33.0	37.6	32.0
2.5	4.1	25.4	5.1	4.6	32.6	29.1	33.7	29.7
3.0	4.1	25.8	5.1	5.9	37.5	31.7	37.5	30.0

EP). The core temperature in this case is 73.1 ºC. Adding enough pitch to fill the entire area outside the winding lowers this by 5 ºC, adding 40% to the life. However, a pitchless extended cathode design drops the core an additional 7 ºC to 61.4 ºC. No other construction changes, including doubling the can bottom thickness, wall thickness, arbor rod, etc. are of much help, with the exception of the core winding [13] technique, which allows the pitch/EP design performance to approach that of the pitchless/EC design. Although more expensive than extended cathode and not always feasible due to volume restrictions, this technique is useful in improving performance in capacitor designs that would normally have empty space around the winding. This space is instead occupied by additional winding area by first winding many "dead" turns of cathode and paper at the beginning of the winding process before introducing the anode. The core winding technique is successful due not as much by having a conductive core as by moving the active, power-generating area outward to an area of larger radius, and by placing the outer area of the winding in closer radial proximity to the can wall. If a core winding is combined with a high-compression extended cathode, the core temperature can be further reduced by 4-5 ºC versus either technique alone.

Table VI
Modeled Temperatures
Various Capacitor Constructions

Construction	Tcore	Tbottom	Tside
P/EP	68.1	54.0	52.0
NP/EP	73.1	55.0	52.0
NP/EC	61.4	56.5	52.5
NP/AR/EC	61.2	56.5	51.5
P/CW/EP	62.2	53.0	52.5
NP/CW/EC	57.5	54.0	52.0
NP/EC/HS	54.4	49.0	49.0
NP/EP/HS	68.4	52.0	51.0
NP/EP/CW/HS	59.9	51.5	51.5
NP/EC/CW/HS	56.0	52.2	51.0
NP/EC/DB	61.0	56.0	51.5
NP/EC/DB/DW	59.8	54.5	52.5
NP/EC/DB/DW/AT	58.8	54.0	52.0

Legend
P=10 W, D=3.0", L=5.63", Winding D=2.55", Ta = 45 ºC, v=2 m/s
EC— Extended Cathode
EP— Extended Paper
HS— Heat Sink aty capacitor bottom, ID=1.2", OD=3.0", Theta = 1.0 ºC/W plus 1.0 ºC/W contact resistance
CW— Core Winding: Inactive 1.4" inactive diameter (paper and cathode only). Winding OD=2.90"
P— Outside of winding is filled completely with pitch
NP— Contains no pitch. Outside of winding is empty.
AR— Aluminum arbor rod. Diameter = 0.3".
AT— Aluminum top.
DW— Double the can wall thickness.
DB— Double the can bottom thickness.

Additional improvement in capacitor performance can be achieved through the use of a heat sink, especially when the capacitor construction is extended cathode, the thermal contact is intimate, and the heat sink thermal resistance is low.

VIII. Conclusions

We have explored the issues and theory behind thermal modeling of aluminum electrolytic capacitors and have developed and presented a model that has simulation and predictive value.

References

[1] Greason, W. D., Critchley, John, "Shelf-life evaluation of aluminum electrolytic capacitors." IEEE Transactions on Components, Hybrids, and Manufacturing Technology, vol. 9, no. 3, September 1986, pp. 293-299.

[2] Incropera, F. P., DeWitt, D. P., Introduction to Heat Transfer. John J. Wiley and Sons, New York, 1985, pp. 669-687.

[3] Incropera, F. P., DeWitt, D. P., *ibid*, p. 35.

[4] Unattributed, "Aavid Forced Air Thermal Calculator." Aavid Engineering, Inc., 1987.

[5] Eisaian, A., "Air-cooling electronic systems: an introduction." Electronic Design, December 1997.

[6] Hsu, T. H., Engineering Heat Transfer. D. Van Nostrand Company, Inc., Princeton, 1963, p. 269.

[7] Lienhard, J. H., A Heat Transfer Textbook. Prentice-Hall, Englewood Cliffs, NJ, 1981, p. 285.

[8] Incropera, F. P., DeWitt, D. P., Fundamentals of Mass and Heat Transfer. John J. Wiley and Sons, New York, 1996, p. 371.

[9] Gasperi, M. L., Gollhardt, N., "Heat transfer model for capacitor banks." 33rd Annual Meeting of the IEEE IAS, October 1998.

[10] Incropera, F. P., DeWitt, D. P., Introduction to Heat Transfer. John J. Wiley and Sons, New York, 1985, p. 609.

[11] Incropera, F. P., DeWitt, D. P., *ibid*, pp. 403-404.

[12] Catalog of Indek Corporation, 1998.

[13] Stevens, J. L., Shaffer, J. S., "Modeling and improving heat dissipation from large aluminum electrolytic capacitors: II." 32nd Annual Meeting of the IEEE IAS, October 1997, pp. 1046-1051.